Available online at www.sciencedirect.com
ScienceDirect
Energy Reports 8 (2022) 48–60
www.elsevier.com/locate/egyr

6th Annual Centre for Doctoral Training Conference in Energy Storage and Its Applications, 2022

Improving performance of fully scalable, flexible transparent conductive films made from carbon nanotubes and ethylene-vinyl acetate

Bernd K. Sturdza[a], Andreas E. Lauritzen[a], Suer Zhou[a], Andre J. Bennett[a], Joshua Form[a], M. Greyson Christoforo[a], Robert M. Dalgliesh[b], Henry J. Snaith[a], Moritz K. Riede[a], Robin J. Nicholas[a,*]

[a] *Department of Physics, Clarendon Laboratory, University of Oxford, Parks Road, Oxford, OX1 3PU, UK*
[b] *ISIS, Rutherford Appleton Laboratory, Chilton, OX11 0QX, UK*

Received 5 May 2022; accepted 13 May 2022
Available online 6 June 2022

Abstract

We report process improvements for the fabrication of single-walled carbon nanotube ethylene-vinyl acetate transparent conductive films. CNT:EVA films demonstrate high resilience against folding and can replace the external dopant in a spiro-OMeTAD based hole selective contact of n-i-p perovskite solar cells achieving a steady-state efficiency of 16.3%. The adapted process is fully scalable, and compared to previous reports (Mazzotta et al., 2018) lowers the material cost dramatically and improves DC to optical conductivity ratio by two orders of magnitude to $\sigma_{dc}/\sigma_{op} = 3.6$ for pristine and $\sigma_{dc}/\sigma_{op} = 15$ for chemically doped films. We analyse the microstructure of our films via small angle neutron scattering and find a positive correlation between the long range packing density of the CNT:EVA films and the σ_{dc}/σ_{op} performance. Increasing monomer ratio and chain length of the EVA polymer improves resilience against bending strain, whereas no significant effect on the CNT wrapping and electrical conductivity of resulting films is found.

Peer-review under responsibility of the scientific committee of the 6th Annual Centre for Doctoral Training Conference in Energy Storage and Its Applications, 2022.

Keywords: Carbon nanotubes; Transparent conductive film; Ethylene-vinyl acetate; Solution processing; Spray coating; Perovskite solar cell; Small angle neutron scattering

1. Introduction

In the past two decades, carbon nanotubes (CNTs) have drawn large scientific and industrial interest due to their outstanding optical, electronic and mechanical properties [1]. These make CNTs a promising candidate for a

* Corresponding author.
E-mail address: robin.nicholas@physics.ox.ac.uk (R.J. Nicholas).

https://doi.org/10.1016/j.egyr.2022.05.047

Peer-review under responsibility of the scientific committee of the 6th Annual Centre for Doctoral Training Conference in Energy Storage and Its Applications, 2022.

variety of applications, such as touch panels, light emitting diodes and photovoltaics [2]. Particularly their long-term stability and flexibility has driven efforts to replace costly and brittle indium tin oxide (ITO) in transparent conductive films [3], as due to the crystalline structure of metal oxides their performance is inherently poor in the emerging field of flexible and stretchable optoelectronic devices [4,5]. During the past decade, various other candidates including graphene, silver nanowires, conducting polymers and metal mesh have been investigated [4,6–10]. However, like ITO these materials struggle with poor cost-performance ratios and meeting requirements of modern optoelectronic devices [11,12], whereas CNTs benefit from the ability to produce more stable flexible films with higher mechanical strength than competitor materials [13].

One of the fundamental parts of most optoelectronic devices are transparent conductive films (TCFs). Commonly, their performance is described by a figure of merit (FoM) that is given by the ratio of the optical and dc conductivities σ_{dc}/σ_{op} [14]. This ratio can be derived from the relation between transmittance (T) and sheet resistance (R_s),

$$T = \left[1 + \frac{Z_0}{2R_s}\frac{\sigma_{op}}{\sigma_{dc}}\right]^{-2}, \tag{1}$$

where Z_0 is the impedance of free space ($Z_0 = 377\ \Omega$), σ_{dc} is the bulk dc conductivity and σ_{op} is the optical conductivity, typically taken at 550 nm [15].

Recent advances in synthesis and doping have propelled CNTs back to the forefront of research by achieving FoMs of above 80 that approach the 350 achieved with ITO [16,17]. Even though CNTs can be synthesised from cheap abundant sources of carbon, the consequent processing cannot be scaled up easily. Typically, for high performance films, CNTs are collected on cellulose filters right after growth and then deposited on substrates via dry transfer [18]. For large scale applications, solution processing is required instead. A large amount of effort has been put into overcoming the inherent tendency of CNTs to agglomerate to large bundles that make them practically useless. Non-covalent functionalisation via polymer wrapping has emerged as the most promising approach to stabilise individual nanotubes in solution. The attractive van der Waals forces between single nanotubes can be suppressed by the side chains of the polymers wrapping the CNTs. Typically, this is done with conjugated polymers like poly(3-hexylthiophene) (P3HT), where the binding interaction between polymer and CNTs is expected to be driven by $\pi - \pi$ or $\pi-$CH stacking [19].

In a previous study we have shown that the insulating non-conjugated co-polymer ethylene-vinyl acetate (EVA) allows dispersion of individual CNTs in organic solvents and consequent deposition of CNT:EVA thin films [20]. EVA offers a range of beneficial properties, such as its low cost, high mechanical and chemical resilience and low water vapour transmission rate [21]. EVA is widely used in industry and the standard encapsulant for silicon solar cell modules.

In this study we attempt to bridge the gap between high performance and cheap large-scale availability of CNT TCFs. By process optimisation and changing the dispersion technique we dramatically decrease the material cost of CNT:EVA films to around 2 €/m^2 (excluding solvents) and develop a fully scalable preparation routine that allows deposition on arbitrary substrates at 100 °C. We investigate the effect of the preparation route on resulting CNT:EVA thin films via Raman spectroscopy, scanning electron microscopy (SEM) and small angle neutron scattering (SANS). The cost of our films is extremely low compared to e.g. CNT:P3HT based films (∼900 €/m^2). [22] We explore the impact of EVA monomer ratio and molecular weight on the selectivity of CNT wrapping, TCF performance and film resilience upon bending. To demonstrate applicability, we combine our CNT:EVA films in a hybrid hole transport layer (HTL) with spiro-OMeTAD in perovskite solar cells. This removes the need for extrinsic p-doping to enhance the conductivity of spiro-OMeTAD, which is known to cause rapid device degradation [23].

2. Results and discussion

2.1. Process optimisation

Charge transport within CNT networks is limited by large inter-tube junction resistances that dominate over the resistance along the tube axis [24,25]. To achieve high transmittance at low sheet resistances it is therefore preferable to increase tube length while avoiding bundling of tubes [26,27]. Standard dispersion protocols for carbon nanotubes typically involve ultra sonication, which is limited to small volumes and has been shown to shorten CNTs [28]. In contrast, shear force mixing is a process that can readily be scaled up to industrial volumes. We thus adapted

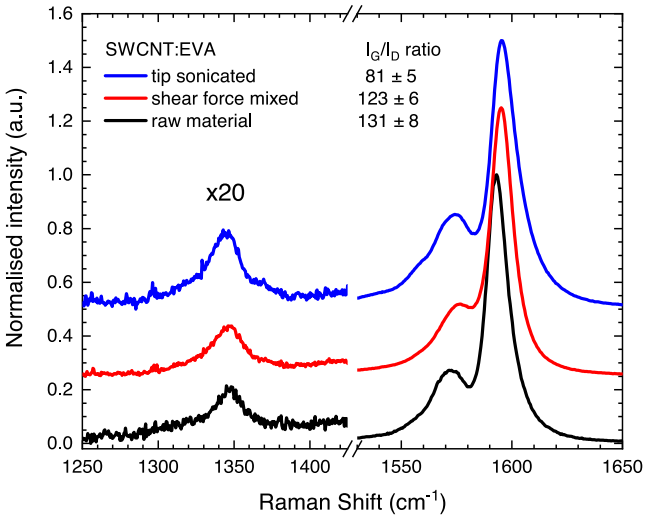

Fig. 1. Raman spectra showing the disorder (1340 cm^{-1}) and graphitic (1590 cm^{-1}) modes of Tuball SWCNTs before and after processing with EVA polymer. (For interpretation of the references to colour in this figure legend, the reader is referred to the web version of this article.)

our preparation routine to employ shear force mixing and increase the batch volume from 10 to 100 mL CNT:EVA solution, corresponding to 0.3 m^2 of film at 85% T.

To investigate the effect of our processing on the carbon nanotubes we perform Raman spectroscopy. Two of the CNT typical modes are the disorder (D) and graphitic (G) modes at 1340 cm^{-1} and 1590 cm^{-1}, respectively. The disorder mode represents a second order scattering process that is enhanced by defects in the nanotube structure. The graphitic band is a tangential C–C stretching vibration and as a first order scattering peak unaffected by defects [29]. Therefore, the G/D peak intensity ratios in Fig. 1 can be used as an indicator of structural CNT quality. We find that the G/D ratio decreases from a value of 131 ± 8 for the Tuball SWCNT raw material down to 123 ± 6 for 48 h shear-force mixed and 81 ± 5 for 10 min tip sonicated samples. This indicates that shear force mixing produces CNT:EVA dispersions with lower defect densities than tip sonication, which is in agreement with literature [28]. Further, the G-band position is blue-shifted to 1595 cm^{-1} in EVA wrapped CNTs compared to the CNT raw material (1593 cm^{-1}). We speculate that the non-covalent attachment of EVA to CNTs causes an increase in the elastic constant of the harmonic oscillator of the polymer-wrapped CNTs [30,31]. A similar shift can be observed in the second peak of the G band, the G$^-$ mode, shifting from 1572 cm^{-1} to 1574 cm^{-1} upon polymer wrapping. The position of this mode correlates with CNT diameter, suggesting the dominant SWCNT species are about 1.7 ± 0.2 nm in diameter [32]. Overall, our Raman data shows that both preparation routes produce SWCNT:EVA films with high structural CNT quality.

The centrifugation step following dispersion, see Section 4, is designed to separate solubilised tubes from bundles, but has been shown to precipitate other impurities, like metal catalysts, contained in the CNT raw material as well. We found that in a CNT raw material purity range of 80–95 wt% the purity had no effect on the quality of our films. This self-purifying nature of our processing demonstrates robustness against impurities and the low purity required significantly lowers the cost of CNT raw material. Combined with the negligible cost of EVA, the material cost of our films is thus reduced to 2 €/m^2. The cost of solvents is excluded as it strongly depends on the chosen concentration and any solvent-recycling scheme used.

Due to the insulating nature of EVA, removing as much of it as possible while preserving CNT solubility is crucial for TCF performance. We thus adapted the excess polymer removal step developed by Schuettfort et al. and Mazzotta et al. [20,33] as described in Section 4 and repeated it once more. The effect of successful polymer removal can be observed in the scanning electron microscopy maps in Fig. 2. The optimised processing yields films with a lower EVA content and smaller CNT bundles (right) than the original process (left).

While SEM images allow visualisation of film morphology, they represent only a small fraction of the film with limited statistical information. Therefore, we performed small angle neutron scattering (SANS), which provides

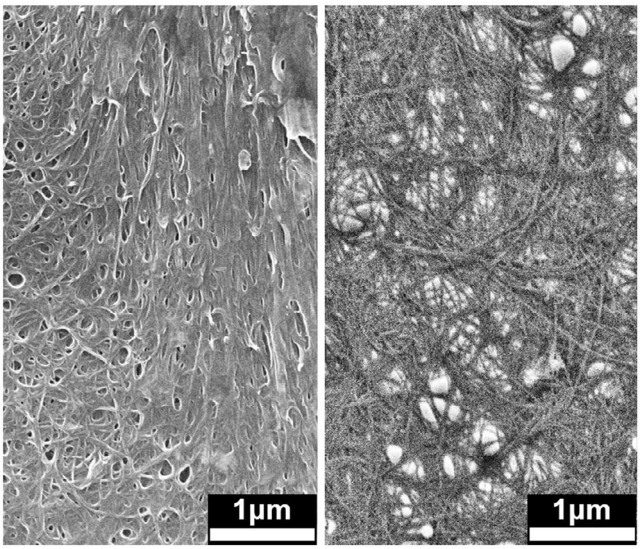

Fig. 2. Scanning electron microscope images of SWCNT:EVA films prepared before (left) and after (right) process optimisation.

insights into sample structure averaged over large volumes of the bulk sample. SANS is able to probe the internal structure of CNT:polymer composites due to the natural scattering length density contrast between the hydrogen-rich polymer and the hydrogen-deficient CNTs [34]. The SANS in this work covers length scales between approximately 10 and 100 nm in the substrate plane. Accessing this information requires fitting of scattering data, for detailed information see Appendix A.1.

Porod plot analysis of ($\log(I)$ vs. $\log(Q)$), where I is the integrated neutron scattering intensity and Q is reciprocal length, shows linear regions that can be described well by either one or two power law fits and point to hierarchical fractal systems. Linear scattering regimes with Porod exponents between 2 and 3 correspond to mass fractals and are typical of the branched multi-level clusters formed by CNT:Polymer composites. We find this to be in good agreement with the branched networks visible in the SEM images in Fig. 2 (right). Higher Porod exponents between 3 and 4 represent surface fractals with exponents close to 3 corresponding to a rough surface and exponents close to 4 to a smooth surface. A more densely packed system will generally result in a higher exponent [35,36].

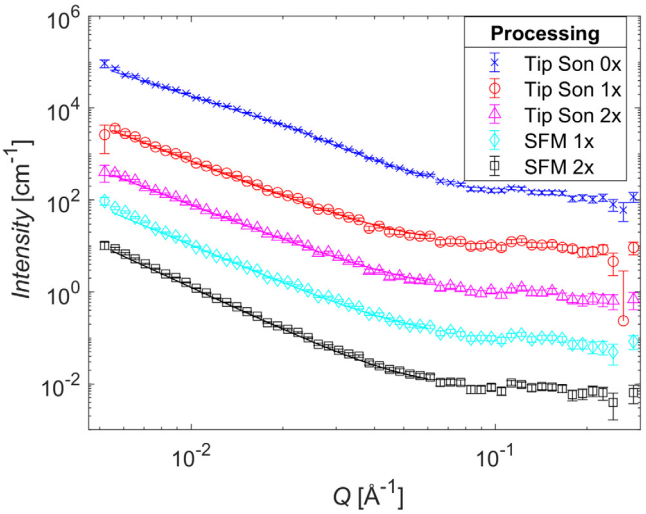

Fig. 3. Porod plot (log(Q) vs. log(I)) of SANS data and power law fits for SWCNT:EVA samples with different processing history. Data sets have been shifted vertically for the sake of clarity.

Table 1. Porod exponents of power law fits for tip sonicated (tip son) and shear force mixed (SFM) samples with different numbers of polymer removal steps. Parameter uncertainties of the last digit are given in brackets.

Dispersion technique	Polymer removal	P	TCF FoM σ_{dc}/σ_{op}
Tip son.	0	2.12 (2)	0.17 (2)
Tip son.	1	2.59 (2)	0.84 (5)
Tip son.	2	2.54 (2)	1.5 (3)
SFM	1	2.76 (2)	1.7 (1)
SFM	2	3.06 (2)	2.1 (2)

SANS data of thin film samples prepared via either tip sonication or shear force mixing and subjected to a given number of excess polymer removal steps is shown in a Porod plot ($\log(I)$ vs. $\log(Q)$) in Fig. 3. The derived Porod exponents and corresponding TCF film performance in σ_{dc}/σ_{op} together with uncertainties in the last digit are presented in Table 1.

We find that the 0x tip sonicated sample appears as having two linear regimes with Porod exponents P and P_{highQ}, representing larger and smaller length scales, respectively. Having two distinct linear regimes could indicate that the composite structure is non-identical at different length scales as observed in prior studies of CNT:polymer composites [36]. The two regimes could also be due to scattering contributions from the excess matter that is removed in the purification process as the samples where polymer has been removed can be represented by a single Porod exponent P.

The tip sonicated sample without polymer removal has a low Q exponent of $P = 2.12$ (2) and a high Q exponent of $P_{highQ} = 2.84$ (5) possibly suggesting that the smallest components of the branching network are relatively denser. We hypothesise the higher scattering and background intensities can be attributed to the presence of larger quantities of hydrogen containing polymer in the sample. This results in a larger background at high Q values due to the increased incoherent scattering of neutrons.

When excess polymer is removed from the samples, only a single structural level is seen. The Porod exponent for both 1x and 2x polymer removal tip sonicated samples is close to 2.5, the expected value of a randomly branched object [37]. We note that this exponent differs from both regimes of the tip sonicated sample without polymer removal, indicating that this step not only removes matter, but also changes the average structure of the scattering film. The small difference between 1x and 2x polymer removed samples further suggests that subsequent polymer removal steps affect the structure of tip sonicated samples to a relatively small degree. The structural change induced by polymer removal is accompanied by a better TCF performance, improving the FoM from $\sigma_{dc}/\sigma_{op} = 0.17 \pm 0.02$ by a factor of 5 after one and by a factor of 9 after two polymer removal steps.

For the SFM samples, we found Porod exponents of 2.76 (2) and 3.06 (2) for 1x and 2x polymer removal. The higher P values of the SFM samples show that the packing is more structurally dense and the films have a more tightly packed mesh than the tip sonicated samples.

Unlike the tip sonicated films, removing polymer for the 2nd time seems to change the structure of the SFM samples. The Porod exponent increases from 2.76 (2) to 3.06 (2), indicating the packing has become so dense that the scattering arises from a rough surface fractal interface, although we note that the fitted values are close to the boundary region between mass and surface fractals [38].

Overall, a tighter packing, expressed in a higher P value, appears to be connected to better TCF performance. This trend can be approximated by a linear relation between σ_{dc}/σ_{op} and P, see A.6. We suspect that denser packing has a positive effect on the number of CNT–CNT junctions and could lower their resistance, thereby increasing the electrical conductivity of the CNT film.

In summary, we have replaced the dispersion technique and optimised the centrifugation and excess polymer removal steps. The improved processing reported here led to a champion FoM of $\sigma_{dc}/\sigma_{op} = 3.6 \pm 0.1$ for CNT:EVA thin films, a factor of 20 higher than previously reported [20]. By chemical doping with chloroauric acid ($HAuCl_4$) as reported by Tsapenko et al. [16], we can further improve the FoM to $\sigma_{dc}/\sigma_{op} = 15 \pm 1$, which is comparable to PEDOT:PSS. However, $HAuCl_4$ doping costs about two orders of magnitude more per area than the material of our films. Finding low-cost alternatives to gold based dopants is therefore a key challenge towards large-scale application of carbon nanotubes.

2.2. Versatility and durability

Optoelectronic devices have application specific requirements on TCF performance, but just as well on flexibility, durability and adaptability that many transparent electrode materials struggle to meet [5,11]. A key aspect in this regard and in TCF preparation in general, is the deposition method. For solution processed materials, which are preferred by industry, several deposition techniques have been demonstrated, such as aerosol jet [39], hydrographic printing [40] and spray coating [41]. We have chosen spray coating as it is an inexpensive, high-throughput and scalable technique that is compatible with low temperature deposition on arbitrary substrates [42].

The most common issue with spray coating is the coffee ring effect and there is a range of parameters to consider in order to prevent it [43]. We find that with our custom-made open science hardware spray coater [44] and the parameters described in Section 4, we achieve highly uniform deposition with standard deviations of the sheet resistance typically below 5% across films. When depositing on different substrates with our system, we find that the spray conditions for ideal film performance can be optimised by changing a single parameter, the nozzle height. This allows deposition of films with performances of up to $\sigma_{dc}/\sigma_{op} = 15 \pm 1$ (doped) on glass and PET substrates, but CNT:EVA films can be sprayed on virtually any substrate like plastics, tape, or paper. Resulting sheet resistances depend on individual surface properties, but even on rough surfaces like weighing paper R_s increased only by a factor of two. Our films perform well above the $\sigma_{dc}/\sigma_{op} = 0.6 \pm 0.1$ that has been demonstrated for spray coated graphene-PEDOT:PSS films on 3D substrates recently [43]. However, our current setup does not allow deposition on 3D surfaces yet.

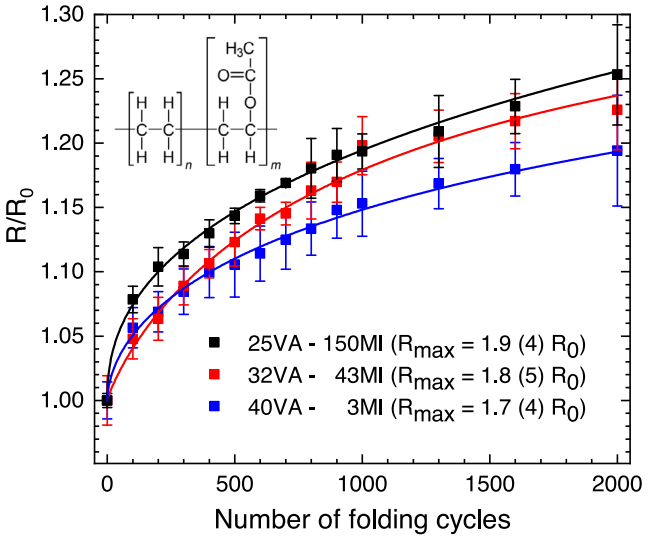

Fig. 4. Change of sheet resistance compared to initial sheet resistance R_0 for up to 2000 folding cycles of SWCNT:EVA films with different EVA polymers on PET. The data follows a logistic function with upper bound R_{max}.

As a co-polymer, EVA consists of chains of monomers ethylene and vinyl-acetate (VA) as displayed in Fig. 4. The properties of EVA can be tuned by changing the monomer weight ratio and the polymer chain length. A higher wt% of VA will decrease the crystallinity and result in a lower tensile strength, stiffness modulus and chemical resistance, but at the same time enhance optical clarity and stress crack resistance [45,46]. Due to the polar nature of the acetoxy side chain, a higher VA content will increase polarity of the copolymer and as a consequence enhance compatibility with polar resins, specific adhesion and printability [45]. In industrial plastics such as EVA, the polymer chain length is described by the melt index (MI) which is inversely related to the molecular weight. Longer chains, or lower MI values, result in a higher viscosity, higher chemical resistance and improved mechanical properties, but detrimental effects on solubility and processability [45]. These tuning factors give EVA a high versatility that is reflected in its typical applications, ranging from shoe soles, cable insulation or drug delivery to electrodes for flexible supercapacitors in CNT:EVA composites [45–47].

To investigate the range of VA content and polymer chain length that can be used for making CNT:EVA thin films, we have prepared samples with five different types of EVA with 25−40%wt VA content and melt indices from

3–150. At lower VA percentages EVA becomes insoluble in chlorobenzene and incompatible with our processing. The five polymers used did not have any significant effect on the TCF performance of the resulting thin films, as is to be expected from the insulating nature of EVA.

Raman scattering from Radial breathing modes shows that the full 1.2–2.0 nm range of CNT diameters contained in the SWCNT raw material is present in all of the films.

In order to test the durability of our films in flexible applications, we performed 2000 folding cycles on CNT:EVA films on PET made from three different EVA batches, see Fig. 4. The bending radius was 2 mm. Sheet resistance measurements were taken along the line of highest bending strain. As outlined above, EVA polymers with higher VA content and lower MI values are expected to perform better in flexible applications. Therefore, we compare three EVA batches that represent the full range of these two parameters. We find that all samples perform well under folding. After an initial increase, the resistance changes less with more cycles, following a logistic function. We find that films with higher VA content and lower melt index perform better and use global fitting to estimate the upper bound of the sheet resistance R_{max}, which is below 2 times the initial value for all three samples. Details of the fits are given in Appendix A.2.

EVA has proven to be a versatile dispersant of CNTs, whose properties can be tuned according to the desired application. Resulting CNT:EVA films can be deposited on a wide range of substrates via scalable spray-coating and perform well in flexible applications.

2.3. Application in PV devices

We use our CNT:EVA films in the hole transport layer (HTL) of perovskite solar cells to showcase their excellent charge transport properties. CNTs remove the requirement of lithium-based dopants in HTLs based on 2,2′,7,7′-tetrakis[N,N-di(4-methoxyphenyl)amino]-9,9′-spiro-bifluorene (spiro-OMeTAD) that have been found to cause rapid device degradation [23,48]. We fabricate analogous devices as Mazzotta et al. but with $FaPbI_3$ as the absorber material [20]. The JV curves of the best devices are shown in Fig. 5 together with their stabilised maximum power efficiencies (PCEs).

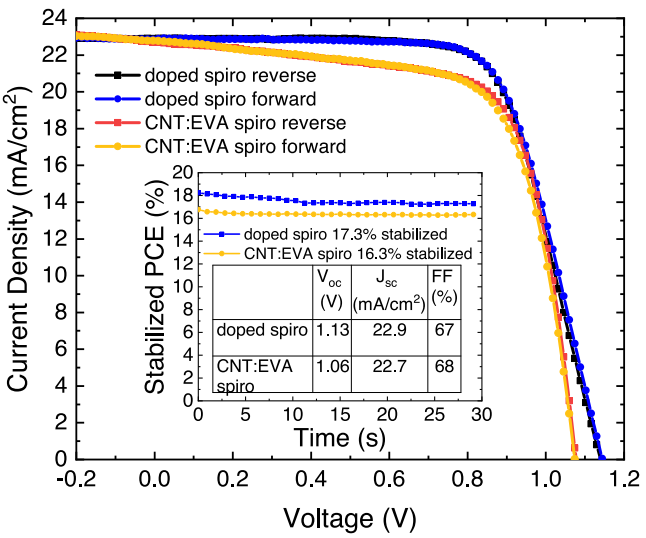

Fig. 5. Current–voltage curves and stabilised maximum power efficiencies of the best perovskite solar cell devices. Devices are identical apart from the hole transport layer, which consisted of CNT:EVA and spiro-OMeTAD (CNT spiro) or Li-TFSI doped spiro-OMeTAD (doped spiro).

The short circuit current density (J_{sc}) is basically unaffected by replacing lithium bis-(trifluoromethanesulfonyl) imide (Li-TFSI) dopant with a 20 nm CNT:EVA layer, demonstrating the excellent transport properties of the hybrid hole selective contact. Additional control devices with just undoped spiro-OMeTAD as HTL did not show the rectifying behaviour typical for a diode, but had the JV curve of a resistor instead.

The lower open circuit voltage (V_{oc}) and the lower shunt resistance (R_{sh}) of the CNT device reduce the stabilised power conversion efficiency from 17.3% for the control to 16.3%. This is the highest stabilised PCE reported for devices incorporating CNT:EVA layers to this date, highlighting the positive effect of improved CNT:EVA film performance. The shunt resistance in the CNT:EVA device is $R_{sh} = 0.55$ k Ω cm^2 compared to $R_{sh} = 14$ k Ω cm^2 in the doped spiro control, calculated from linear fits to the J–V curves at the short circuit point. This is due to the high surface roughness of the CNT film. Reducing the surface roughness of carbon nanotube films remains a key challenge in the field and is beyond the scope of this work.

We also tested chemical doping with $HAuCl_4$ in the CNT:EVA layer in PV devices, but to date this does not show any significant improvement. The J–V characteristics suggest that device performance is not limited by the film conductivity and the introducing of gold doping is not needed, thus enabling undoped CNT:EVA films to be used in low cost device fabrication routes.

3. Conclusions

Scalable processing of individualised carbon nanotubes is one of the main obstacles preventing their large-scale application in optoelectronics. The modified preparation process we present in this work offers a low-cost route to scalable solution processing and spray deposition of carbon nanotubes. Our modifications have improved the transparent conductive film performance of our CNT:EVA films dramatically, achieving $\sigma_{dc}/\sigma_{op} = 15$. We have analysed the effect of different processing conditions on the microstructure of our films via small angle neutron scattering, revealing that a higher long range packing density correlates with a better TCF performance of our films, likely due to an increased density of CNT–CNT junctions. Comparing EVA polymers with different vinyl acetate contents and chain lengths showed that these parameters do not affect CNT wrapping or TCF performance of resulting CNT:EVA films. However, we found that polymers with higher VA content and longer chains are more resilient against folding and bending. This demonstrates that the type of EVA polymer can be chosen as preferred to optimise the mechanical properties while leaving the electronic properties of the composite film unaffected. The films can be used in the hole transport layer of perovskite solar cells, removing the necessity of doping spiro-OMeTAD extrinsically and achieving a stabilised maximum power efficiency of 16.3%, which is the highest value reported for devices incorporating CNT:EVA layers to date.

4. Experimental methods

CNT:EVA Solution Preparation. The solution processing for tip sonicated samples is as described by Mazzotta et al. [20]. Samples for comparison of different EVA polymers were prepared identically using Elvax 4355, 4320, 150, 40 W and 40L-03 (DuPont). For shear force mixed samples, 40 mg of EVA pellets (ELVAX 150, Dupont 32%wt vinyl acetate comonomer content, unless otherwise noted) were dissolved in 100 mL chlorobenzene (Acros Organics, ACS reagent grade) by stirring at 50 °C overnight. 40 mg of Tuball SWCNTs (OCSiAl, 80% or 93% grade) were added to the solution and it was shear force mixed for 48 h at 10 000 rpm (Silverson L5M-A) while kept at a constant temperature of 28 °C. The mixture was then centrifuged at 10 000 g for 8 min and the supernatant collected. The precipitate containing impurities and non-functionalised CNTs was discarded. The supernatant was added to 200 mL of toluene and placed on a hotplate at 50 °C for 24 h to cause aggregation of nanotubes while keeping excess EVA polymer dissolved. After cooling back to room temperature, the mixture was centrifuged at 16 000 g for 4 min or until the supernatant was fully transparent. The precipitate now contains pellets of functionalised carbon nanotubes, while excess EVA is removed with the supernatant. This excess polymer removal step is repeated once more and the CNT:EVA pellets are then dissolved in 500 mL of chloroform (Acros Organics, for HPCL grade, stabilised with 25 ppm amylene). This dispersion is stable for weeks and CNT aggregates can easily be broken up by a brief dispersion treatment prior spray deposition.

Conductive Film Deposition. CNT:EVA films were spray coated with a custom-built open science hardware setup.

PET or glass substrates were prepared as described in Ref. [20].

Chemical Doping of CNT/EVA films. 60 mg of tetrachloroauric(III) acid trihydrate ($HAuCl_4{\cdot}3H_2O$, Alfa Aesar, ACS grade, 99.99%) were dissolved in 40 ml of ethanol (Merck, ACS grade) at 50 °C and consequently aerosolized by an OMRON compressor nebuliser NE-C801 as described in [16].

Solar Cell Materials. Formamidinium iodide (FAI) (>99.99%) was purchased from Greatcell Solar Materials. PbI_2 (99.999%) and PbBr2 (>98.0%) were purchased from TCI. Methylammonium bromide (MABr) was

purchased from Xi'an Polymer Light Technology Corp. Methylammonium chloride (MACl), potassium chloride (KCl) and phenethylammonium iodide (PEAI) were purchased from Sigma-Aldrich. 2,2′,7,7′-tetrakis(N,N′-di-p-methoxyphenylamine)-9,9′-spirobifluorene (Spiro-OMeTAD) (>99.5%) was obtained from Lumtech. Lithium bis-(trifluoromethanesulfonyl)imide (Li-TFSI, >99%), 4-tert-butylpyridine (tBP, 98%), Isopropanol (IPA, 99.5%), N, N-dimethylformamide (DMF, anhydrous 99.8%), dimethyl sulfoxide (anhydrous DMSO, >99.9%), anisole (anhydrous, 99.7%), chlorobenzene (CB, 99.8%), acetonitrile (ACN, anhydrous 99.8%) were purchased from Sigma-Aldrich. Chemicals were used as received without further purification. Gold pellets for evaporation were purchased from Kurt J. Lesker.

Solar Cell Fabrication. Solar cells were prepared as described in [20] with the following modifications. The FTO substrates (Pilkington Tec7) were cleaned by subsequently sonicating in Decon 90 solution (1% vol. in D.I. water), D.I. water, acetone, isopropanol for 10 min each. Afterwards, the substrates were dried in a continuous stream of nitrogen gas and UV-ozone cleaned for 15 min before SnO_2 layer deposition. The SnO_2 chemical bath deposition was done following the same methods as described in [20]. KCl was used to passivate the SnO_2 layer. Briefly, 20 mM of KCl solution in D.I. water was made and spin coated onto the substrates at 3000 rpm for 30 s. Then the substrates were dried on the hotplate at 100 °C for 10 min. The substrates were UV-ozone cleaned for another 15 min before the perovskite film deposition. 1.6M FAPbI3 99% with 35% excess MACl and 1% MAPbBr3 additive was used as the absorber material. The chemicals were dissolved in 4:1 DMF:DMSO and stirred on the hotplate at room temperature for 1 h. Then 100 μL of precursor solution was drop-casted on the substrate and spun at 6000 rpm for 30 s (3000 rpm/s ramp speed). 300 μL of anisole was dripped onto the substrate 10 s into the spinning program. The perovskite films were then annealed at 150 °C for 15 min. After the perovskite layer deposition, a 5 mM PEAI was dissolved in isopropanol and spin coated onto the perovskite layer for passivation. The PEAI solution was drop-casted onto the substrate dynamically spinning at 3000 rpm for 30 s. The substrates were then either spray-coated with CNT:EVA on top or left as they were for the control devices. For the control devices with doped spiro-OMeTAD, 85 mg of spiro-OMeTAD was dissolved in 1 mL chlorobenzene. Then 33 μl of tert-butyl pyridine (tBP) and 20 μl of Li-TFSI (520 mg/mL in acetonitrile) were added to the spiro-OMeTAD solution. For the devices with undoped spiro-OMeTAD, 85 mg of spiro-OMeTAD was dissolved in 1 mL chlorobenzene. Then only 33 μl of tBP was added to the spiro-OMeTAD solution. After depositing the CNT:EVA layers (or perovskite control), 60 μl of doped or undoped spiro-OMeTAD solution was dropped onto the substrates spinning at 2000 rpm for 30 s. Afterwards, 80 nm gold electrodes were evaporated onto the samples under vacuum of $< 9 \cdot 10^{-9}$ bar.

Current–Voltage (J–V) Measurements. The photovoltaic devices were characterised in ambient condition with the room temperature around 20–24 °C and 45% relative humidity under AM1.5G simulated sunlight generated by a class AAA WaveLabs Sinus-220 solar simulator, using a Keithley 2400 source meter. The intensity of the solar simulator was set to produce 100 mW/cm^2 equivalent irradiance using a certified KG3-filtered Si reference photodiode (Fraunhofer ISE). The voltage was swept at a rate of 0.61 V/s first from forward bias to reverse bias (forward sweep) followed by a reverse sweep in the opposite scan direction. The minimum voltage was −0.1 V and the maximum voltage was 1.2 V. On each substrate, there were 3 devices with an area 0.25 cm^2 and 1 larger device with an area of 1.00 cm^2. The areas were defined using black anodised aluminium shadow masks in direct contact with the glass side of the substrates within enclosed sample holders. The equivalent solar irradiance used for power conversion efficiency calculations was estimated before each solar cell measurement run based on the integrated spectrum of the solar simulator's internal spectrometer compared to the integrated value measured at the same time as its intensity was set using the certified reference photodiode. The equivalent irradiance was found to be in the range 0.985–1.004 suns, which has been applied to calculate power conversion efficiencies.

Transmittance Measurements. Transmittance data was acquired with a PerkinElmer LAMBDA 1050 UV–vis–NIR spectrophotometer using 2 nm steps.

Sheet Resistance Measurements. 4-point tungsten carbide probes from Jandel Engineering (0.634 mm spacing) and a Keithley 2450 source meter were used to measure sheet resistance. A sweep current from −0.2 to 0.2 mA was applied across the outer probes while the voltage across the inner probes was measured. The slope of the current–voltage data corrected with the factor $\pi/ln(2)$ for the in line configuration was used to calculate the sheet resistance. For each sample, five spots across the film were measured and averaged.

Raman Spectroscopy. Raman spectra were acquired with a Jobin Yvon T64000 triple spectrometer and an Andor DU420A-OE CCD. The spectrometer was calibrated with the 520.7 cm^{-1} line of a Silicon wafer. Samples were excited with a Ventus solo Nd:YAG laser ($\lambda = 532$ nm) or a Melles griot He:Ne laser ($\lambda = 633$ nm). **SEM Maps** were taken with a Hitachi S-4300 SEM at an accelerating voltage of 17 kV.

Small angle neutron scattering (SANS) was done at the Larmor beamline at the ISIS Neutron and Muon Source. Samples were measured using neutrons with $dQ/Q = 8\%$ and a wavelength range of 0.9–13.5 Å with an unpolarised square beam of dimensions 6.6 mm × 6.6 mm to avoid uneven film edges. The collected Q ($Q = 4\pi/\lambda \cdot sin(\theta/2)$) range was 0.0052 to 0.67 $Å^{-1}$, but only data from 5.5×10^{-3} $Å^{-1}$ to 6×10^{-2} $Å^{-1}$ was considered structurally relevant. Sample illumination time was approximately 4 h to ensure sufficient counts were recorded. Samples were measured in aluminium containers with 0.5 mm thick quartz entry and exit windows (Quartz type "WHQ" from Knight Optical) which is chosen due to its low contribution to coherent scattering. Film coating was done as described above. The measured sample configurations consisted of 10 quartz substrates (same type as used for the container windows) coated with about 150 nm of CNT:EVA composite each as well as 6 spacer substrates to fit the geometry of the container all stacked on top of each other. This was done to increase the scattering sample volume due to the low thickness of the films. Sample scattering was normalised by subtraction of scattering from 16 uncoated substrates in a container as well the empty beam.

Declaration of competing interest

The authors declare the following financial interests/personal relationships which may be considered as potential competing interests: Moritz K Riede, Robin J Nicholas has patent #UK Patent Application 1719915.9 pending to Oxford University Innovation Limited.

Acknowledgements

B.K.S. acknowledges EPSRC for the funding through the Centre for Doctoral Training in New and Sustainable PV (EP/L01551X/1) and University College, Oxford, for the Oxford-Radcliffe scholarship. A.E.L. thanks EPSRC for funding through the Doctoral Training Partnership (EP/N509711/1) as well as STFC and the ISIS Neutron and Muon facility and project (1948713). S.Z. thanks the Rank Prize Funds for their funding in her Ph.D. studies. We thank the STFC ISIS Neutron and Muon Facility for access to neutron scattering facilities (session RB2010523) [49]. This work benefited from the use of the SasView application, originally developed under National Science Foundation award DMR-0520547. SasView contains code developed with funding from the European Union's Horizon 2020 research and innovation programme under the SINE2020 project, grant agreement No 654000.

Notes

The authors declare the following competing financial interest(s): M.K.R., and R.J.N. are inventors on the UK Patent Application 1719915.9, (date of filing: 30 November 2017) regarding the process described in this work.

Appendix. Sample appendix section

A.1. Small angle neutron scattering (SANS)

SANS data was analysed in SASView [50]. Initial Porod plot ($\log(Q)$ vs. $\log(I)$) analysis showed one or two linear regions, pointing to a hierarchical, fractal system. Similar systems also displaying fractal behaviour [36] are often described in terms of the multiscale Beaucage model [51,52]. We were not successful in applying this model due to the four different fitting parameters per level making the physical interpretations of the fit values difficult and the investigated Q-range not covering the low Q Guinier regime. Instead, data showing one linear regime was fitted as a power law

$$I(q) = scale \cdot q^{-P} + background \tag{A.1}$$

where P is the Porod exponent and the scale and background are empirical fitting parameters. The background of fits were determined by fitting a constant value for the intensity between $1–3 \cdot 10^{-1}$ $Å^{-1}$. Scattering data showing two linear regimes were fitted as

$$I(q) = \begin{cases} A\, q^{-P} + background, & q \leq q_c \\ B\, q^{-P_{highQ}} + background, & q > q_c, \end{cases} \tag{A.2}$$

where P, P_{highQ} are the Porod exponents, q_c the cross over point between the regimes and A and B are scaling constants with $B = A q_c^{P_{highQ}} / q_c^{P}$ to ensure the values match at the boundary. Reported parameter uncertainties correspond to those calculated by the DREAM algorithm which used for fitting.

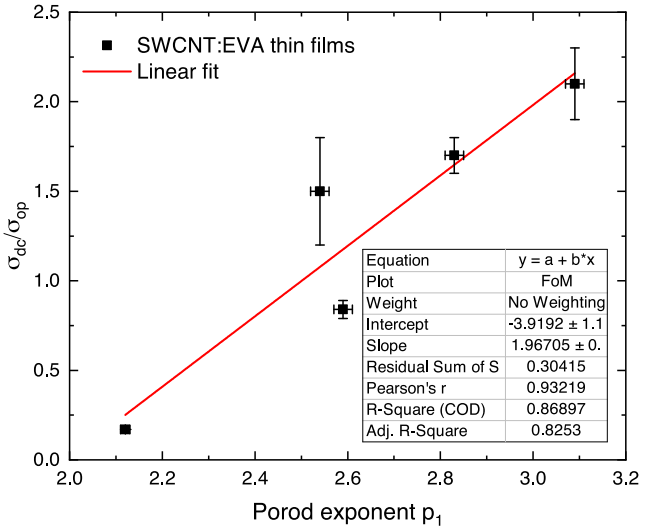

Fig. A.6. TCF figure of merit σ_{dc}/σ_{op} as a function of the low Q Porod exponent P extracted from small angle neutron scattering with a linear fit.

A.2. Logistic fits of folding cycle data

The relative sheet resistance R/R_0 data was fitted with a logistic function in a global fit. The initial value A_1 is by definition equal to 1. The parameters for centre position x_0 and power p are shared between the three sets of data, whereas the upper bound A_2 is fitted individually. Details of the fit are shown in Fig. A.7.

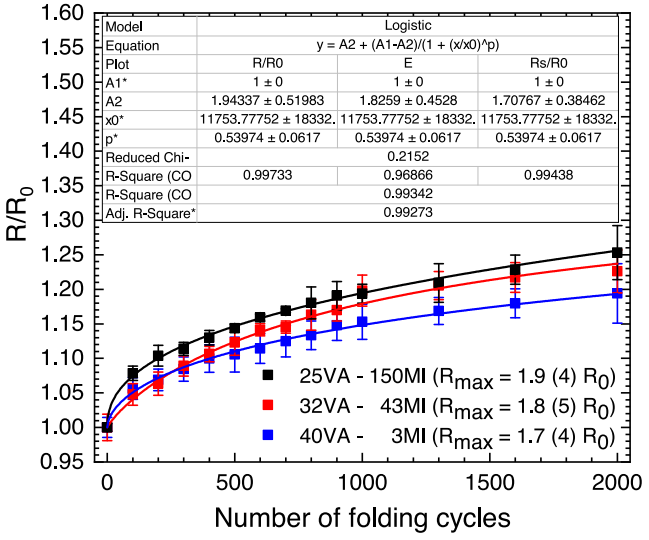

Fig. A.7. Change of sheet resistance compared to initial sheet resistance R_0 for up to 2000 folding cycles of SWCNT:EVA films with different EVA polymers on PET. The data follows a logistic function with upper bound R_{max}.

References

[1] Baughman RH, Zakhidov AA, De Heer WA. Carbon nanotubes - the route toward applications. Science 2002;297(5582):787–92. http://dx.doi.org/10.1126/science.1060928.

[2] Hecht DS, Hu L, Irvin G. Emerging transparent electrodes based on thin films of carbon nanotubes, graphene, and metallic nanostructures. Adv Mater 2011;23(13):1482–513. http://dx.doi.org/10.1002/adma.201003188.
[3] Kumar A, Zhou C. The race to replace tin-doped indium oxide: Which material will win? ACS Nano 2010;4(1):11–4. http://dx.doi.org/10.1021/nn901903b.
[4] McCoul D, Hu W, Gao M, Mehta V, Pei Q. Recent advances in stretchable and transparent electronic materials. Adv Electron Mater 2016;2(5):1–51. http://dx.doi.org/10.1002/aelm.201500407.
[5] Zhao S, Li J, Cao D, Zhang G, Li J, Li K, Yang Y, Wang W, Jin Y, Sun R, Wong CP. Recent advancements in flexible and stretchable electrodes for electromechanical sensors: Strategies, materials, and features. ACS Appl Mater Interfaces 2017;9(14):12147–64. http://dx.doi.org/10.1021/acsami.6b13800.
[6] Guo CF, Ren Z. Flexible transparent conductors based on metal nanowire networks. Mater Today 2015;18(3):143–54. http://dx.doi.org/10.1016/j.mattod.2014.08.018.
[7] Ye S, Rathmell AR, Chen Z, Stewart IE, Wiley BJ. Metal nanowire networks: The next generation of transparent conductors. Adv Mater 2014;26(39):6670–87. http://dx.doi.org/10.1002/adma.201402710.
[8] Hecht DS, Hu L, Irvin G. Emerging transparent electrodes based on thin films of carbon nanotubes, graphene, and metallic nanostructures. Adv Mater 2011;23(13):1482–513. http://dx.doi.org/10.1002/adma.201003188.
[9] Ellmer K. Past achievements and future challenges in the development of optically transparent electrodes. Nature Photon 2012;6(12):809–17. http://dx.doi.org/10.1038/nphoton.2012.282.
[10] Du J, Pei S, Ma L, Cheng HM. 25Th anniversary article: Carbon nanotube- and graphene-based transparent conductive films for optoelectronic devices. Adv Mater 2014;26(13):1958–91. http://dx.doi.org/10.1002/adma.201304135.
[11] Chang NL, Ho-Baillie AWY, Vak D, Gao M, Green MA, Egan RJ. Manufacturing cost and market potential analysis of demonstrated roll-to-roll perovskite photovoltaic cell processes. Sol Energy Mater Sol Cells 2018;174(August 2017):314–24. http://dx.doi.org/10.1016/j.solmat.2017.08.038.
[12] Emmott CJ, Urbina A, Nelson J. Environmental and economic assessment of ITO-free electrodes for organic solar cells. Sol Energy Mater Sol Cells 2012;97:14–21. http://dx.doi.org/10.1016/j.solmat.2011.09.024.
[13] Yu L, Shearer C, Shapter J. Recent development of carbon nanotube transparent conductive films. Chem Rev 2016;116(22):13413–53. http://dx.doi.org/10.1021/acs.chemrev.6b00179.
[14] Coleman JN, De S, King PJ, Lyons PE, Khan U. Size effects and the problem with percolation in nanostructured transparent conductors. Acs Nano 2010;4(12):7064–72. http://dx.doi.org/10.1021/nn1025803.
[15] Glover ER. Conductivity of superconducting films for photon energies between 0.3 and 40k T. Phys Rev 1957;108:243–56. http://dx.doi.org/10.1017/s0017383500002710.
[16] Tsapenko AP, Romanov SA, Satco DA, Krasnikov DV, Rajanna PM, Danilson M, Volobujeva O, Anisimov AS, Goldt AE, Nasibulin AG. Aerosol-assisted fine-tuning of optoelectrical properties of SWCNT films. J Phys Chem Lett 2019;10(14):3961–5. http://dx.doi.org/10.1021/acs.jpclett.9b01498.
[17] He L, Tjong SC. Nanostructured transparent conductive films: Fabrication, characterization and applications. Mater Sci Eng R Rep 2016;109:1–101. http://dx.doi.org/10.1016/j.mser.2016.08.002.
[18] Kaskela A, Nasibulin AG, Timmermans MY, Aitchison B, Papadimitratos A, Tian Y, Zhu Z, Jiang H, Brown DP, Zakhidov A, Kauppinen EI. Aerosol-synthesized SWCNT networks with tunable conductivity and transparency by a dry transfer technique. Nano Lett 2010;10(11):4349–55. http://dx.doi.org/10.1021/nl101680s.
[19] Fujigaya T, Nakashima N. Non-covalent polymer wrapping of carbon nanotubes and the role of wrapped polymers as functional dispersants. Sci Technol Adv Mater 2015;16(2):24802. http://dx.doi.org/10.1088/1468-6996/16/2/024802.
[20] Mazzotta G, Dollmann M, Habisreutinger SN, Christoforo MG, Wang Z, Snaith HJ, Riede MK, Nicholas RJ. Solubilization of carbon nanotubes with ethylene-vinyl acetate for solution-processed conductive films and charge extraction layers in perovskite solar cells. ACS Appl Mater Interfaces 2018;11:acsami.8b15396. http://dx.doi.org/10.1021/acsami.8b15396.
[21] Barber GD, Jorgensen GJ, Terwilliger K, Glick SH, Pern J, McMahon TJ. New barrier coating materials for PV module backsheets. In: Conference record of the IEEE photovoltaic specialists conference. 2002, p. 1541–4. http://dx.doi.org/10.1109/pvsc.2002.1190906.
[22] As an indication we report current prices in UK from sigmaaldrich.com: SWCNT 1.3 nm dia: 1150 £/g, rr-P3HT: 511 £/g, EVA (vinyl acetate 25 wt %) 0.50: £/g and price of the 80% purity Tuball SWCNT we used from tuball.com: 3 £/g.
[23] Habisreutinger SN, Leijtens T, Eperon GE, Stranks SD, Nicholas RJ, Snaith HJ. Carbon nanotube/polymer composites as a highly stable hole collection layer in perovskite solar cells. Nano Lett 2014;14(10):5561–8. http://dx.doi.org/10.1021/nl501982b.
[24] Fuhrer MS, Nygård J, Shih L, Forero M, Yoon YG, Mazzoni MS, Choi HJ, Ihm J, Louie SG, Zettl A, McEuen PL. Crossed nanotube junctions. Science 2000;288(5465):494–7. http://dx.doi.org/10.1126/science.288.5465.494.
[25] Stadermann M, Papadakis SJ, Falvo MR, Novak J, Snow E, Fu Q, Liu J, Fridman Y, Boland JJ, Superfine R, Washburn S. Nanoscale study of conduction through carbon nanotube networks. Phys Rev B 2004;69(20):10–2. http://dx.doi.org/10.1103/PhysRevB.69.201402.
[26] Jiang S, Hou PX, Chen ML, Wang BW, Sun DM, Tang DM, Jin Q, Guo QX, Zhang DD, Du JH, Tai KP, Tan J, Kauppinen EI, Liu C, Cheng HM. Ultrahigh-performance transparent conductive films of carbon-welded isolated single-wall carbon nanotubes. Sci Adv 2018;4(5). http://dx.doi.org/10.1126/sciadv.aap9264.
[27] Mustonen K, Laiho P, Kaskela A, Zhu Z, Reynaud O, Houbenov N, Tian Y, Susi T, Jiang H, Nasibulin AG, Kauppinen EI. Gas phase synthesis of non-bundled, small diameter single-walled carbon nanotubes with near-armchair chiralities. Appl Phys Lett 2015;107(1). http://dx.doi.org/10.1063/1.4926415.
[28] Graf A, Zakharko Y, Schieß l SP, Backes C, Pfohl M, Flavel BS, Zaumseil J. Large scale, selective dispersion of long single-walled carbon nanotubes with high photoluminescence quantum yield by shear force mixing. Carbon 2016;105:593–9. http://dx.doi.org/10.1016/j.carbon.2016.05.002.

[29] Dresselhaus MS, Dresselhaus G, Saito R, Jorio A. Raman spectroscopy of carbon nanotubes. Phys Rep 2005;409(2):47–99. http://dx.doi.org/10.1016/j.physrep.2004.10.006.
[30] Adam AJ, Lenehan CE, Quinton JS. Parametric analysis of sonication and centrifugation variables for dispersion of single walled carbon nanotubes in aqueous solutions of sodium dodecylbenzene sulfonate. Carbon 2011;49(15):5213–28. http://dx.doi.org/10.1016/j.carbon.2011.07.039.
[31] Sinani VA, Gheith MK, Yaroslavov AA, Rakhnyanskaya AA, Sun K, Mamedov AA, Wicksted JP, Kotov NA. Aqueous dispersions of single-wall and multiwall carbon nanotubes with designed amphiphilic polycations. J Am Chem Soc 2005;127(10):3463–72. http://dx.doi.org/10.1021/ja045670+.
[32] Telg H, Duque JG, Staiger M, Tu X, Hennrich F, Kappes MM, Zheng M, Maultzsch J, Thomsen C, Doorn SK. Chiral index dependence of the G + and G - Raman modes in semiconducting carbon nanotubes. ACS Nano 2012;6(1):904–11. http://dx.doi.org/10.1021/nn2044356.
[33] Schuettfort T, Snaith HJ, Nish A, Nicholas RJ. Synthesis and spectroscopic characterization of solution processable highly ordered polythiophene-carbon nanotube nanohybrid structures. Nanotechnology 2010;21(2). http://dx.doi.org/10.1088/0957-4484/21/2/025201.
[34] Sivia D. Elementary scattering theory for X-ray and neutron users. Oxford University Press; 2011.
[35] Schaefer DW, Justice RS. How nano are nanocomposites? Macromolecules 2007;40(24):8501–17. http://dx.doi.org/10.1021/ma070356w.
[36] Tehrani M, Etampawala TNB, Dadmun M, Hossain MA. Resolving hierarchical structures in carbon nanotube networks using small- and ultrasmall-angle neutron scattering. J Phys Chem C 2017;121(40):22442–51. http://dx.doi.org/10.1021/acs.jpcc.7b06114.
[37] Schaefer DW, Brown JM, Anderson DP, Zhao J, Chokalingam K, Tomlin D, Ilavsky J. Structure and dispersion of carbon nanotubes. J Appl Crystallogr 2003;36(3 I):553–7. http://dx.doi.org/10.1107/S0021889803005028.
[38] Beaucage G. Small-angle scattering from polymeric mass fractals of arbitrary mass-fractal dimension. J Appl Crystallogr 1996;29(2):134–46. http://dx.doi.org/10.1107/S0021889895011605.
[39] Jabari E, Toyserkani E. Micro-scale aerosol-jet printing of graphene interconnects. Carbon 2015;91:321–9. http://dx.doi.org/10.1016/j.carbon.2015.04.094.
[40] Zhang Y, Gui Y, Meng F, Li L, Gao C, Zhu H. Graphene water transfer printing for 3D surface. In: The 29th IEEE international conference on micro electro mechanical systems (MEMS 2016) (January). Beijing, China: National Key Laboratory of Nano / Micro Fabrication Technology; 2016, p. 13–6.
[41] Krebs FC. Fabrication and processing of polymer solar cells: A review of printing and coating techniques. Sol Energy Mater Sol Cells 2009;93(4):394–412. http://dx.doi.org/10.1016/j.solmat.2008.10.004.
[42] Lefebvre V, Arthur McDonell. Atomization and sprays. 2017.
[43] Carey T, Jones C, Le Moal F, Deganello D, Torrisi F. Spray-coating thin films on three-dimensional surfaces for a semitransparent capacitive-touch device. ACS Appl Mater Interfaces 2018;10(23):19948–56. http://dx.doi.org/10.1021/acsami.8b02784.
[44] AFMD. LANDS - large area nanoparticle deposition system. 2022, http://afmd.github.io/LANDS (accessed Feb 18, 2022).
[45] Henderson AM. Ethyl- vinyl acetate (EVA) copolymers: A general review. IEEE Electr Insul Mag 1993;9(1):30–8.
[46] Salyer IO, Kenyon AS. Structure and property relationships in ethylene–vinyl acetate copolymers. J Polym Sci A-1 1971;9(11):3083–103. http://dx.doi.org/10.1002/pol.1971.150091101.
[47] Guan X, Kong D, Huang Q, Cao L, Zhang P, Lin H, Lin Z, Yuan H. In situ growth of a high-performance all-solid-state electrode for flexible supercapacitors based on a PANI/CNT/EVA composite. Polymers 2019;11(1):178. http://dx.doi.org/10.3390/polym11010178.
[48] Habisreutinger SN, Wenger B, Snaith HJ, Nicholas RJ. Dopant-free planar n-i-p perovskite solar cells with steady-state efficiencies exceeding 18%. ACS Energy Lett 2017;2(3):622–8. http://dx.doi.org/10.1021/acsenergylett.7b00028.
[49] Riede MK, et al. Domain size and purity in the active layers of vacuum deposited organic solar cells. STFC ISIS Neutron Muon Source 2020. http://dx.doi.org/10.5286/ISIS.E.RB2010523.
[50] Doucet M, et al. SasView Version 4.2.2, Zenodo. http://dx.doi.org/10.5281/zenodo.2652478.
[51] Beaucage G. Approximations leading to a unified exponential/power-law approach to small-angle scattering. J Appl Crystallogr 1995;28(6):717–28. http://dx.doi.org/10.1107/s0021889895005292.
[52] Hammouda B. Analysis of the beaucage model. J Appl Crystallogr 2010;43(6):1474–8. http://dx.doi.org/10.1107/S0021889810033856.